Research Article | Vol. 27, No. 2 | 21 Jan 2019 | OPTICS EXPRESS 1099

Optics EXPRESS

Jitter detection based on parallax observations and attitude data for Chinese Heavenly Palace-1 satellite

HAIQIU LIU,[1,*] HUIMIN MA,[1] ZHAOHUI JIANG,[1] AND DEJIE YAN[2]

[1]*School of Information and Computer, Anhui Agricultural University, 130 Changjiang West Road, Hefei 230036, China*
[2]*Changchun Institute of Optics, Fine Mechanics and Physics, Chinese Academy of Sciences, 3888 Nanhu road, Changchun 130033, China*
[*]*hqliu2018@hotmail.com*

Abstract: Parallax observations from staggered charge-coupled devices (CCDs) have been applied to satellite jitter detection. Nevertheless, the jitter during the initial period of an imaging process cannot be detected. This paper presents an approach that combines parallax observations with the attitude data from attitude-measuring sensors in order to detect the global jitter, including the initial jitter. Low-frequency components, which can be reconstructed from attitude data, account for most jitter energy, and determine the jitter curve's overall shape. We introduce attitude data into parallax observations to constrain the initial jitter and find its optimum estimate. Meanwhile, an offset is extracted from parallax observation images by using a comprehensive matching method. A mathematical model is developed to demonstrate how to calculate the global jitter with the initial jitter and offset. Numerical simulation results indicate that, for pixel-level offset error, the root-mean-square error (RMSE) of the proposed method is 1.4 pixels, while the measurement error near integer multiples of characteristic frequency is amplified significantly. Experiments performed on Chinese Heavenly Palace-1 satellite show that the jitter at 0.12Hz with an amplitude about 6 pixels exists in the cross-track direction, while the down-track jitter results fail to show obvious periodicity.

1. Introduction

The stability of satellite platform is an essential factor for the imaging performance of an optical satellite [1]. Nevertheless, it is disturbed by various attitude oscillations. Although most of the motion can be suppressed or isolated by attitude regulators or vibration isolators, there is still some residual jitter left [2,3], and the jitter is usually with relatively smaller amplitudes and wider frequency span of hundreds of Hertz [4,5]. The jitter can be transmitted to cameras via the satellite platforms, causing unnecessary image motion on the focal planes, and ultimately resulting in image distortions [6–19]. As the spatial resolution of optical satellites increases, the focal length of cameras get longer, the images consequently become more sensitive to the jitter [20,21]. Thus, it has become essential to develop a method to detect the jitter for high-resolution optical satellites.

The detection of satellite jitter has been studied in some researches, which can be categorized into three approaches.

The first approach is dependent on a high-performance attitude-measuring sensor which can collect the jitter information with a high sampling rate and high accuracy [22,23]. For example, the Angular Displacement Assembly (ADA) installed on Landsat-7 spacecraft measured the jitter every 2 milliseconds [24], and the high-frequency angular displacement sensor equipped on Chinese Yaogan-26 satellite detected the platform jitter at a frequency range of 0.2~450 Hz [4]. High-performance attitude measurement sensors have been

#351302 https://doi.org/10.1364/OE.27.001099
Journal © 2019 Received 7 Nov 2018; revised 22 Dec 2018; accepted 26 Dec 2018; published 14 Jan 2019

employed on some high-resolution satellites, but they are still technically unavailable for many satellites.

The second approach is to catch the movement of image points by adding an image sensor on the focal plane. Janschek et al. obtained overlapping images by installing an auxiliary matrix imaging sensor on the focal plane and detected the image motion from the images using an optical correlator [25–27]. This method made full use of the high frame rate of matrix image sensors to capture the movement of image points, and adopted the optical correlator to realize fast image matching.

The third approach is on the basis of parallax observations between two pushbroom sensors that can acquire overlapping images at slightly different times. Mattson et al. investigated the jitter for HiRISE camera from adjacent charge coupled device (CCD) arrays' images [28]. Adapting the same method, Mattson et al. detected the jitter of LROC-NAC camera from overlapping portion of each NACL and NACR images [29]. Teshima and Iwasaki used the relative registration errors between two different bands of ASTER short-wave infrared images to reconstruct an attitude fluctuation of about 1.5 Hz [30,31]. From the inter-image offsets between a pair of slightly canted sensors, Mumtaz and Palmer measured the attitude oscillation of a disaster monitoring constellation [32]. Jiang et al. compensate the attitude errors of ZY1-02C satellite by the use of staggered CCDs [33]. Tong et al. assessed the periodic distortions caused by the attitude oscillation in the ZY-3 satellite by using multispectral and three-line-scanning imagery [34,35]. Sun et al. adopted the same methods as Tong to Chinese mapping satellite-1 and the jitter at 0.1Hz and 0.6 Hz were discovered [36]. Liu et al. retrieved the jitter information of Chinese ZY-3 Satellite from image space discrepancies [37].

The third method has received more attention for its independence from extra high-performance attitude-measuring devices or imaging sensors. The overlapping parts in parallax observation images are essential for this method to detect jitter [28–37]. However, in a shooting mission, there is a short period of time during which staggered CCDs cannot produce overlapping images, leading to the difficulty in detecting the jitter of the corresponding period.

The fact is that although the jitter has a wide frequency span of hundreds of Hertz, the low-frequency components account for the majority of its energy [2], determining the overall shape of the jitter curve, and can be reconstructed from the attitude data of attitude-measuring sensors [38].

Therefore, this paper combines the parallax observation images and attitude data to detect the jitter throughout a shooting mission, including the period without overlapping images.

The rest of this paper is organized as follows. Following the introduction, Section 2 presents the fundamentals of the proposed method. The distribution of the period without overlapping images in a shooting mission is first introduced. Then a time-domain jitter detection model is developed to make it clear that the jitter during the period without overlapping images can be used to calculate the global jitter. Section 3 presents the whole methodology of jitter detection. A comprehensive image matching strategy combining image alignment, NCC and quadric surface fitting is used to extract a sub-pixel offset series from overlapping images. The jitter in the period without overlapping images is then assessed by an approach based on both the offset series and the attitude data from attitude-measuring sensors. Section 4 analyzes the detectable frequencies and the accuracy of the proposed method by numerical simulations. Following this, experiments performed to validate the proposed approach on Chinese Heavenly Palace-1 satellite are described in Section 5. Finally, the conclusions are given in Section 6.

2. Fundamental

2.1 Distribution of period without overlapping images

In a pushbroom system with several CCDs mounted on the focal plane, two staggered CCDs usually overlaps each other on the edges by dozen columns of pixels [39–41], which give rise to overlapping footprints of the same size in the object plane. The overlapping footprints turn out to be the overlapping area in images from the overlapping CCDs, as shown in Fig. 1. Due to the distance of L lines between the two staggered CCDs in the scanning direction, the two overlapping parts scan the same target with a fixed time interval of τ. Most of the two images from the overlapping parts are overlapped with each other, whereas the first L lines in the upper CCD image, which are acquired in the initial period of τ in an imaging process, do not overlap with the lower CCD image. Similarly, the last L lines in the lower CCD image, acquired in the final τ, do not overlap with the upper CCD image. For Chinese Heavenly Palace-1 satellite, the time interval of τ accounts for over 7% of an imaging process.

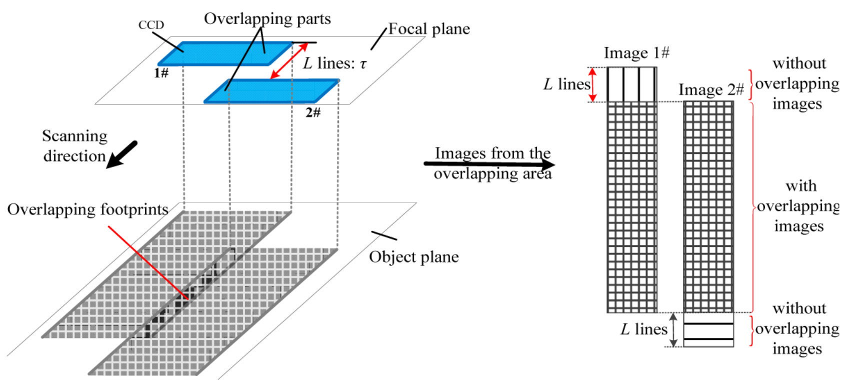

Fig. 1. Distribution of overlapping images and non-overlapping images.

2.2 Development of jitter detection model

Due to the distance between the two staggered CCDs, the two overlapping parts shoot the same target at slightly different times, while they are affected by the same jitter simultaneously [21], causing a deviation of the same target's position in the two overlapping images, as shown in Fig. 2.

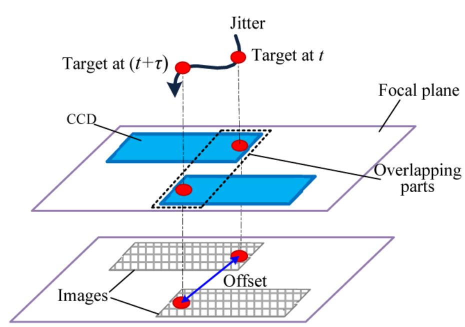

Fig. 2. Process of one object images in two adjacent TDICCDs with jitter.

According the imaging principle of overlapping areas, the relationship between the jitter and the offset is expressed as:

$$g(t+\tau) = j(t+\tau) - j(t), \qquad 0 \le t \le T - \tau, \tag{1}$$

Optics EXPRESS

Where $j(t)$ is the jitter function, and $j(t+\tau)$ is the same jitter function translated by the fixed observation time lag τ, $\tau = L \times T_r$, L denotes the difference between the two adjacent CCDs in the scanning direction, T_r is the image line time, $g(t+\tau)$ denotes the offset between the image obtained by the lower CCD at time t and that obtained by the upper CCD at time $(t+\tau)$, and T is the duration of a shooting mission.

Given that the offset obtained from images is typically a discrete time series, Eq. (1) need to be discretized as follows:

$$j(r+R) = j(r) + g(r+R), \qquad r = 1, 2, \cdots N \times R \tag{2}$$

Where $j(r)$ and $j(r+R)$ indicate the jitter at time $r \times T_g$ and $(r+R) \times T_g$, respectively. $g(r+R)$ denotes the offset between the image obtained by the lower CCD at time $r \times T_g$ and that obtained by the upper CCD at time $(r+R) \times T_g$, T_g is the sampling period of the offset series, $R = \lfloor \tau / T_g \rfloor$, and $N = \lfloor T/\tau \rfloor$-1. The operator $\lfloor x \rfloor$ rounds x to the nearest integer less than or equal to x. Equation (2) can be expanded as:

$$\begin{cases} j(r+R\ ) = j(r) + g(r+R) \\ j(r+2R) = j(r) + g(r+R) + g(r+2R) \\ j(r+3R) = j(r) + g(r+R) + g(r+2R) + g(r+3R) \\ \qquad\vdots \\ j(r+NR) = j(r) + g(r+R) + g(r+2R) + \cdots + g[r+NR] \end{cases}, \qquad r = 1, 2, \cdots R \tag{3}$$

In order to establish the jitter estimation model, the jitter and the offset are rewritten as:

$$\mathbf{J}_0 = \left[j(1), j(2), \cdots, j(R) \right]_{1\times R} \tag{4}$$

$$\mathbf{J} = [\mathbf{J}_1, \mathbf{J}_2, \cdots, \mathbf{J}_N]^T = \begin{bmatrix} j(1+R) & j(2+R) & \cdots & j(2R) \\ j(1+2R) & j(2+2R) & \cdots & j(3R) \\ \vdots & \vdots & \vdots & \vdots \\ j(1+NR) & j(2+NR) & \cdots & j(R+NR) \end{bmatrix}_{N\times R} \tag{5}$$

$$\mathbf{G} = [\mathbf{G}_1, \mathbf{G}_2, \cdots, \mathbf{G}_\mathbf{N}]^T = \begin{bmatrix} g(1+R) & g(2+R) & \cdots & g(2R) \\ g(1+2R) & g(2+2R) & \cdots & g(3R) \\ \vdots & \vdots & \vdots & \vdots \\ g(1+NR) & g(2+NR) & \cdots & g(R+NR) \end{bmatrix}_{N\times R} \tag{6}$$

Where $\mathbf{J}_0$ denotes the initial jitter from time 0 to τ in a shooting mission. We establish Eq. (3) to emphasize the relationship between the subsequent jitter $\mathbf{J}$ and the initial jitter $\mathbf{J}_0$ by dividing the total jitter into groups with the same size as initial jitter $\mathbf{J}_0$. Of course, the length of the total jitter may not be an integer multiple of the length of the initial jitter $\mathbf{J}_0$, we only extract the integer multiple part from the total jitter, and the rest can still be calculated using Eq. (2).

According to Eq. (3), the jitter estimation model can be constructed as:

$$\mathbf{J} = \begin{bmatrix} 1 \\ 1 \\ \vdots \\ 1 \end{bmatrix}_{N\times 1} \times \mathbf{J}_0 + \begin{bmatrix} 1 & 0 & & \cdots & 0 \\ 1 & 1 & 0 & \cdots & 0 \\ \vdots & \vdots & \ddots & \ddots & \vdots \\ & & \cdots & 1 & 0 \\ 1 & 1 & & \cdots & 1 \end{bmatrix}_{N\times N} \times \mathbf{G} \tag{7}$$

It can be seen that the initial jitter $\mathbf{J}_0$, which refers to the jitter from 0 to time τ, can be used to calculate the subsequent jitter with the assist of offset data $\mathbf{G}$.

3. Methodology

Figure 3 shows the approach for estimating the jitter using overlapping CCDs' images and attitude data. The approach contains three components, as follows: (1) A comprehensive matching strategy, which combines image alignment, NCC and quadric surface fitting, is used to extract the offset from overlapping CCDs' images. In the strategy, the overlapped images are first aligned according to the layout of overlapping CCDs. The aligned images are then matched using NCC to obtain pixel-level conjugate points. Following this, the accuracy of the conjugate points is further improved by using quadric surface fitting of the correlation coefficients, and the vertex of the surface is regarded as subpixel-level conjugate points. Finally, an offset series is gained by calculating the coordinate difference between the conjugate points. (2) An approach is proposed to estimate the initial jitter from the attitude data and the offset data. Jitter refers to the focal plane's displacement in pixels in the down-track and cross-track directions, while the attitude data refers to the rotation angles of a satellite's yaw, pitch and roll. Therefore, the rotation angles are first converted to the displacement of a satellite's focal plane in the down-track and cross-track directions by using the conversion formula of coordinates. The discrete displacement points are then fitted to generate dense low-frequency initial jitter. What follows are to combine the low-frequency initial jitter with the offset to establish an objective function, which is used to evaluate the smoothness of the deviation from the true initials. Finally, the smoothest solution is found by an optimization algorithm and regarded as the optimal solution of the initial jitter. (3) Substitute the estimated values of the offset and initial jitter into the jitter detection model in Section 3.2 to calculate the jitter. Detailed descriptions of the proposed approach are given in the following sections.

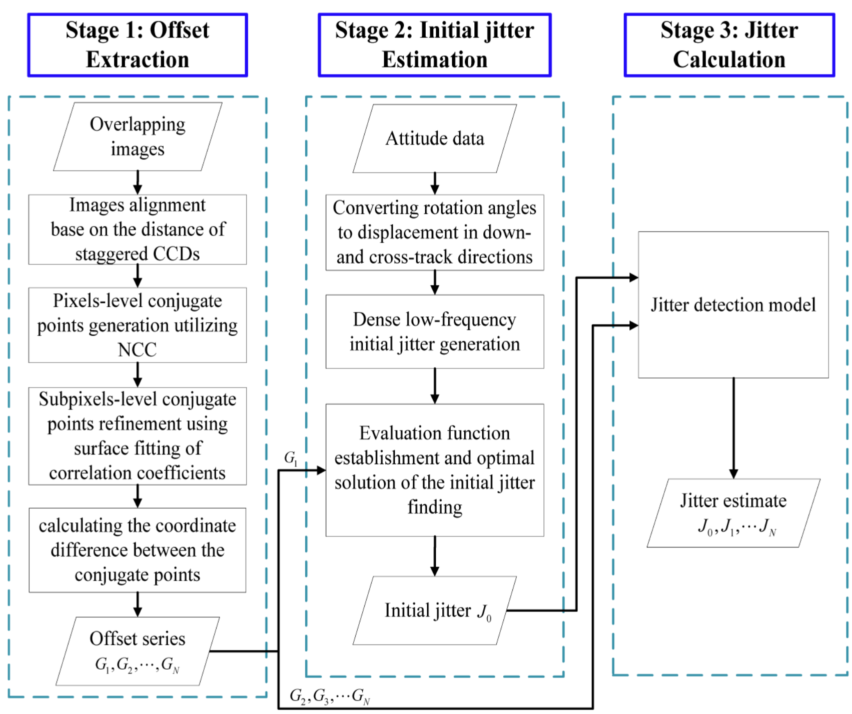

Fig. 3. Framework for detection of the jitter based on overlapping images and attitude data.

Optics EXPRESS

3.1 Extracting offset from overlapping CCDs' images

Due to the distance of L lines between two staggered CCDs, they shoot a target with a fixed time tag, causing the locations of the exact same target in the two overlapping images staggered L lines, as shown in Fig. 1. The distance of L depends on the package of a CCD, it is typically equal to thousands of times the size of a pixel, so it is necessary to align the two images before matching them. The two staggered images can be aligned by eliminating the first L lines in the upper CCD's image and the last L lines in the lower CCD's image. For the Chinese Heavenly Palace-1 satellite, the distance between two adjacent CCDs used for the experiments of this study is 3480 lines.

Offset evaluates the deviation of the same scene's position in two overlapping images, and it can be extracted by matching the aligned images. Normalized cross-correlation (NCC) is a popular method used for remote sensing images registration, however, it usually achieves only pixel-level accuracy [34]. In order to gain sub-pixel accuracy of image matching, a comprehensive image matching strategy combining NCC with quadric surface fitting is used. The specific matching steps are as follows: (1) Registration points are sampled every u image lines, we can provide a dense sampling by reducing the value of u. In the experiments of this study, u was set to 40 lines, equal to the width of the CCD overlaps, so the sampling frequency of registration points was up to 384Hz ($1/(40 \times 65\mu s) = 384Hz$). (2) Reference templates are generated by the neighborhood of $p \times p$ pixels around registration points. NCC is adopted to find the candidate with the maximum correlation coefficient within a search range of $q \times q$ pixels. We can improve the accuracy of conjugate points by increasing the value of p and q. In the experiments in this study, p and q were set to 10 pixels and 40 pixels. (3) Quadric surface fitting for the correlation coefficients is then performed to achieve subpixel-level conjugate points. The least square method is employed to determine the coefficients of the surface with the size of $q \times q$ pixels, and the vertex of the surface is found by using the differential method and taken as the subpixel-level conjugate point. (4) In a pair of conjugate points, the row and column coordinates of one point are subtracted by the corresponding coordinates of the other point to acquire an offset data, then an offset series can be obtained after the subtraction performed on all the conjugate points.

3.2 Estimating initial jitter from attitude data and offset series

Two staggered CCDs shoot a target with a fixed time interval of τ, whereas they are disturbed by the same jitter simultaneously, causing an offset of the target in overlapping images. The offset in overlapping images has been used to detect jitter [28–31]. However, from the beginning time 0 to τ in a shooting mission, the staggered CCDs cannot produce any overlapping images, leading to the difficulty in detecting the jitter in the corresponding period. In this research, the jitter from time 0 to τ is called initial jitter. Therefore, an approach is proposed to estimate the initial jitter from the attitude data and the offset results in Section 3.1, and the details of the approach are described as follows.

(1) Converting rotation angles to displacement of satellite's focal plane

Jitter refers to the focal plane's displacement in the down-track and cross-track directions, while the attitude data is the rotation angles of a satellite's yaw, pitch and roll. Therefore, the rotation angles need to be converted to the displacement of the focal plane in the down-track and cross-track directions first.

$$p(\varphi_i,\theta_i,\psi_i)=\begin{bmatrix}p^d\\p^c\\p^v\\1\end{bmatrix}=\begin{bmatrix}-\Gamma/H-h&0&0&0\\0&-\Gamma/H-h&0&0\\0&0&-\Gamma/H-h&-\Gamma\\0&0&0&1\end{bmatrix}\begin{bmatrix}1&0&0&0\\0&\cos\varphi_i&\sin\varphi_i&0\\0&-\sin\varphi_i&\cos\varphi_i&0\\0&0&0&1\end{bmatrix}\begin{bmatrix}\cos\theta_i&0&-\sin\theta_i&0\\0&1&0&0\\\sin\theta_i&0&\cos\theta_i&0\\0&0&0&1\end{bmatrix}$$
$$\begin{bmatrix}\cos\psi_i&\sin\psi_i&0&0\\-\sin\psi_i&\cos\psi_i&0&0\\0&0&1&0\\0&0&0&1\end{bmatrix}\begin{bmatrix}1&0&0&0\\0&1&0&0\\0&0&1&-(R+H)\\0&0&0&1\end{bmatrix}\begin{bmatrix}\cos\gamma&0&-\sin\gamma&0\\0&1&0&0\\\sin\gamma&0&\cos\gamma&0\\0&0&0&1\end{bmatrix}\begin{bmatrix}\cos i_0&-\sin i_0&0&0\\\sin i_0&\cos i_0&0&0\\0&0&1&0\\0&0&0&1\end{bmatrix}$$
$$\begin{bmatrix}\cos\Omega t&0&\sin\Omega t&0\\0&1&0&0\\-\sin\Omega t&0&\cos\Omega t&0\\0&0&0&1\end{bmatrix}\begin{bmatrix}\cos i_0&\sin i_0&0&0\\-\sin i_0&\cos i_0&0&0\\0&0&1&0\\0&0&0&1\end{bmatrix}\begin{bmatrix}\cos\gamma_0&0&\sin\gamma_0&0\\0&1&0&0\\-\sin\gamma_0&0&\cos\gamma_0&0\\0&0&0&1\end{bmatrix}\begin{bmatrix}1&0&0&0\\0&1&0&0\\0&0&1&(R+H)\\0&0&0&1\end{bmatrix}\begin{bmatrix}u_1\\u_2\\0\\1\end{bmatrix}$$
(8)

Where p^d and p^c denote the image motion in the down-track and cross-track directions, p^v is the motion perpendicular to the focal plane. Γ means the focal length. u_1 and u_2 indicate the distance between the targets and the sub-satellite point. R and Ω denotes the radius and the self-rotation rate of Earth. i_0 and H are the inclination and the height of orbit. γ_0 is the angle between the satellite and the ascending node. h denotes the topographic height of scene. Ψ_i, θ_i and φ_i denote the angles of satellite's yaw, pitch and roll, $i = 1, 2, \ldots, M$, M is the number of Ψ_i, θ_i and φ_i samples.

The conversion formula of coordinates, as shown in Eq. (8), was established by Chinese academician J. Wang, and has been applied to several Chinese satellites, including the Chinese Heavenly Palace-1. Results have proven that with the aid of the conversion formula of coordinates, the rotation angles can be converted to the displacement of a focal plane accurately [42].

It should be noted that the results derived from the conversion formula of coordinates are the image motion on the focal plane. It is mainly composed of three components caused by orbital movement, earth rotation and attitude oscillations. We using the Eq. (9) to extract the component caused by the attitude oscillations.

$$\left(d^d{}_i,d^c{}_i,d^v{}_i\right)=-\left(p^d{}_i,p^c{}_i,p^v{}_i\right)=-\left[p(\varphi_i,\theta_i,\psi_i)-p(\varphi_0,\theta_0,\psi_0)\right],\qquad i=1,2,\cdots M \quad (9)$$

Where Ψ_0, θ_0 and φ_0 denote the initial value of Ψ_i, θ_i and φ_i at the beginning of an imaging process. $d^d{}_i$ and $d^c{}_i$ denote the displacement of the focal plane in the down-track and cross-track directions caused by attitude oscillations, $d^v{}_i$ is the displacement of the focal plane perpendicular to the focal plane, which has been proven to be insignificant [21,37,43]. The proposed jitter detection method in this study is applicable to both the down-track and cross-track directions. Thus in the following contents, the two symbols of low-frequency jitter, $d^d{}_i$ and $d^c{}_i$, are both replaced by d_i.

In addition, the attitude-measuring sensors equipped on most satellites can only provide the attitude data at a relatively low sampling rate. For example, the sampling frequencies of gyro and star sensors installed on LROC-NAC camera were 10Hz and 5Hz [29], respectively, and the on-orbit attitude data for ASTER sensor was updated at a frequency of about 1Hz [30]. As a result, only dozens of sample points can be obtained in a shooting mission, which may be not enough for accurate data fitting.

In order to acquire sufficient samples of the attitude data, we extend the sampling time to the pre-imaging preparation phase. In the experiments of this study, a total of 117 sample points of attitude data $\{d_i\}_{117}$ were obtained from Chinese Heavenly Palace-1 satellite during a 30-second imaging phase and a 30-second pre-imaging preparation phase.

Optics EXPRESS

(2) Generating dense low-frequency initial jitter by fitting

Jitter has been proven to be a time-variable, unpredictable, and periodic phenomenon, and can be characterized by a sum of sinusoidal models [21,44,45], as shown in Eq. (10).

$$d(t)=\sum_{q=0}^{Q}\mathrm{A}_q\sin\left(\omega_q t+\lambda_q\right) \tag{10}$$

Where $d(t)$ denotes the fitting function of low-frequency jitter. A_q, ω_q and λ_q (q = 1, 2,…, Q) are the amplitude, angular frequency and initial phase of the qth sinusoidal model, respectively. Q is the number of sinusoidal models. The value of Q needs to be determined for parameters estimation. In practice, we usually use two or three sinusoidal terms to fit the low-frequency jitter, which is an empirical value, and may vary with different satellites. If you cannot give a reasonable value for the number of sinusoidal models, the following method may provide a possible solution for this issue: Collecting the low-frequency jitter points as much as possible to increase its sample size. Some of them are used as training data with the rest as testing data. Least square method is then performed on the training data to estimate a possible value of Q. For each value between 1 and Q, the corresponding model is obtained by performing the least square method on training data, and its performance on testing data is then evaluated by calculating deviations. The value that minimizes the deviations is used as the optimal estimate of Q.

The unknown parameters $\{A_q\}_Q$, $\{\omega_q\}_Q$ and $\{\lambda_q\}_Q$ are estimated from the low-frequency jitter points $\{d_i\}_\mathrm{M}$ by using the least square method. Then, using the fitting function $d(t)$ of low-frequency jitter, we can calculate the low-frequency initial jitter values $\{d(r)\}_R$ at those times associate with the offset series, $R=\lfloor\tau/T_g\rfloor$, T_g is the sampling period of the offset series.

(3) Establishing an objective function using the initial jitter and offset data

In order to evaluate the relative deviation between the estimated value of jitter and its low-frequency component, an objective function is established based on the minimum variance theory, as shown in Eq. (11).

$$S\left(\mathbf{J}_0\right)=\sum_{r=1}^{R}\left[\frac{j(r)-d(r)}{d(r)}\right]^2+\sum_{r=1}^{R}\left[\frac{j(r)+g(r+R)-d(r+R)}{d(r+R)}\right]^2 \tag{11}$$

Where $\mathbf{J}_0=[\,j(1),j(2),\ldots,j(R)\,]_{1\times R}$, $j(r)$, $d(r)$ and $g(r)$ denote the jitter, the low-frequency jitter and the offset at time $r\times T_g$, respectively.

The objective function measures the smoothness of the deviation from its low-frequency component, the smoothest solution minimizes the objective function, meaning that the smoothest solution approaches the true initial jitter according to the minimum variance theory. The conjugate gradient method is employed to find $\hat{\mathbf{J}}_0$ that minimizes the objective function, and it is regarded as the optimal solution of the initial jitter $\mathbf{J}_0$.

It should be noted that all these are based on the premise that the minimum of the objective function S ($\mathbf{J}_0$) exists, so it is necessary to prove the existence of the objective function's minimum. Based on the theory that a convex function on the real set has a minimum, we judge the existence of the objective function's minimum by analyzing its convexity. The following theorem is often used to determine the convexity of a function: A twice continuously differentiable function is convex on its domain if and only if its Hessian matrix of second partial derivatives is positive definite in its domain. As a L-ary quadratic function, the objective function S ($\mathbf{J}_0$) is twice continuously differentiable, and its Hessian matrix can be expressed as:

Optics EXPRESS

$$\nabla^2 S(\mathbf{J}_0)=\begin{bmatrix}\frac{\partial^2 S(\mathbf{J}_0)}{\partial j(1)^2},\frac{\partial^2 S(\mathbf{J}_0)}{\partial j(1)\partial j(2)},\cdots,\frac{\partial^2 S(\mathbf{J}_0)}{\partial j(1)\partial j(R)}\\ \frac{\partial^2 S(\mathbf{J}_0)}{\partial j(2)\partial j(1)},\frac{\partial^2 S(\mathbf{J}_0)}{\partial j(2)^2},\cdots,\frac{\partial^2 S(\mathbf{J}_0)}{\partial j(2)\partial j(R)}\\ \cdots\cdots\\ \frac{\partial^2 S(\mathbf{J}_0)}{\partial j(R)\partial j(1)},\frac{\partial^2 S(\mathbf{J}_0)}{\partial j(R)\partial j(2)},\cdots,\frac{\partial^2 S(\mathbf{J}_0)}{\partial j(R)^2}\end{bmatrix}_{R\times R} \tag{12}$$

The first partial derivative of the objective function $S(\mathbf{J}_0)$ can be denoted as:

$$\begin{aligned}\frac{\partial S(\mathbf{J}_0)}{\partial j(1)}&=\frac{2}{d(1)^2}\cdot\left[j(1)-d(1)\right]+\frac{2}{d(1+R)^2}\cdot\left[j(1)+g(1+R)-d(1+R)\right]\\ \frac{\partial S(\mathbf{J}_0)}{\partial j(2)}&=\frac{2}{d(2)^2}\cdot\left[j(2)-d(2)\right]+\frac{2}{d(2+R)^2}\cdot\left[j(2)+g(2+R)-d(2+R)\right]\\ \vdots\qquad&\qquad\vdots\qquad\qquad\qquad\vdots\\ \frac{\partial S(\mathbf{J}_0)}{\partial j(R)}&=\frac{2}{d(R)^2}\cdot\left[j(R)-d(R)\right]+\frac{2}{d(R+R)^2}\cdot\left[j(R)+g(R+R)-d(R+R)\right]\end{aligned} \tag{13}$$

Likewise, the second partial derivatives of the objective function $S(\mathbf{J}_0)$ are denoted as

$$\begin{aligned}\frac{\partial S^2(\mathbf{J}_0)}{\partial j(1)\partial j(r)}&=\begin{cases}2\cdot\left(\frac{1}{d(1)^2}+\frac{1}{d(1+R)^2}\right), & r=1\\ 0, & others\end{cases}\\ \frac{\partial S^2(\mathbf{J}_0)}{\partial j(2)\partial j(r)}&=\begin{cases}2\cdot\left(\frac{1}{d(2)^2}+\frac{1}{d(2+R)^2}\right), & r=2\\ 0, & others\end{cases}\\ \vdots\qquad&\qquad\vdots\qquad\qquad\vdots\\ \frac{\partial S^2(\mathbf{J}_0)}{\partial j(R)\partial j(r)}&=\begin{cases}2\cdot\left(\frac{1}{d(R)^2}+\frac{1}{d(R+R)^2}\right), & r=R\\ 0, & others\end{cases}\end{aligned} \tag{14}$$

Then the Hessian matrix $\nabla^2 S(\mathbf{J}_0)$ can be rewritten as:

$$\nabla^2 S(\mathbf{J}_0)=\begin{bmatrix}2\cdot\left(\frac{1}{d(1)^2}+\frac{1}{d(1+R)^2}\right) & 0 & \cdots & 0\\ 0 & 2\cdot\left(\frac{1}{d(2)^2}+\frac{1}{d(2+R)^2}\right) & \cdots & 0\\ \vdots & \ddots & \ddots & \vdots\\ 0 & \cdots & 0 & 2\cdot\left(\frac{1}{d(R)^2}+\frac{1}{d(R+R)^2}\right)\end{bmatrix}_{R\times R} \tag{15}$$

According to Sylvester's criterion, namely a matrix is positive definite if and only if all determinants of its upper-left sub-matrixes are positive, we can test the positive definiteness of the Hessian matrix $\nabla^2 S(\mathbf{J}_0)$. Determinants of its upper-left sub-matrixes can be denote as:

$$\left|\nabla^2 S(\mathbf{J}_0)_{i\times i}\right| = 2^i \cdot \left(\frac{1}{d(1)^2}+\frac{1}{d(1+R)^2}\right)\left(\frac{1}{d(2)^2}+\frac{1}{d(2+R)^2}\right)\cdots\left(\frac{1}{d(i)^2}+\frac{1}{d(i+R)^2}\right),\quad i=1,2,\cdots,R \tag{16}$$

Where $d(1)^2$, $d(2)^2$,…$d(R)^2$, $d(1+R)^2$, $d(2+R)^2$,…$d(R+R)^2$ >0, thus

$$\left|\nabla^2 S(\mathbf{J}_0)_{i\times i}\right| > 0,\quad i=1,2,\cdots,R \tag{17}$$

It can be seen that all the determinants are positive. According to Sylvester's criterion, the Hessian matrix $\nabla^2 S$ ($\mathbf{J}_0$) is a positive-definite matrix, and we can further determine the objective function S ($\mathbf{J}_0$) is convex. According to properties of convex functions, namely a convex function on the real set has a minimum, the objective function S ($\mathbf{J}_0$) has a minimum. The above analysis prove the existence of the objective function's minimum.

3.3 Calculating the jitter using the detection model

The estimated initial jitter j(r: 1≤r≤R) and the offset series g(r: 1≤r≤NR) are first rewritten as Eq. (4) and Eq. (6) to obtain the initial jitter vector $\mathbf{J}_0$ and offset matrix $\mathbf{G}$, then the jitter matrix $\mathbf{J}$ can be obtained according to the Eq. (7).

In summary, we converted the equation between jitter and offset (Eq. (1)) into its matrix form (Eq. (7)) to make it clear that the initial jitter $\mathbf{J}_0$, which refers to the jitter from 0 to time τ, can be used to calculate the subsequent jitter. An approach combining attitude data and parallax observation images was proposed to detect the initial jitter $\mathbf{J}_0$, with which the subsequent jitter can be calculated by using Eq. (7). Compared with the existing method, the proposed method can detect the global jitter throughout a shooting mission, including the initial jitter, in other words, the detectable time range of the proposed method is [0 T], while the existing method's detectable time range is [τ T], where T denotes the duration of a shooting mission. So the detectable time range is expanded.

4. Analysis of detectable frequencies and accuracy

Compared with the existing method which extracts the jitter simply from parallax observation images, the proposed method combines the images and the low-frequency attitude data to detect jitter. The proposed method enable us to estimate the initial jitter, while the existing method cannot. Besides the extended time range, we are also interested in its detectable frequencies and accuracy.

4.1 Analysis of detectable frequencies

In order to investigate the detectable frequencies of the proposed method, we further analyzed the Eq. (1). Since the satellite jitter shows a sinusoidal pattern [21,44,45], the offset derived from the jitter can be expressed by a sum of the sinusoidal models as follows:

$$g(t) = \sum_{k=1}^{K} B_k \sin(2\pi f_k t + \sigma_k) \tag{18}$$

Where f_k, B_k and σ_k are the frequency, amplitude and initial phase of the kth sinusoidal model of the offset, respectively. According to the Eq. (18), the relationships of the corresponding frequencies and amplitudes between the offset and jitter can be constructed as:

$$f'_k = f_k,\quad k=1,2,\cdots,K \tag{19}$$

$$B'_k = \frac{B_k}{\left|2\sin(\pi\cdot\tau\cdot f_k)\right|},\quad k=1,2,\cdots,K \tag{20}$$

Optics EXPRESS

Where f_k' and B_k' are the frequencies and amplitudes of the kth sinusoidal model of the jitter, respectively. The denominator in the Eq. (20) is required to be not equal to zero, thus the frequency f_k'has to meet the condition as follows:

$$f_k \neq \frac{n}{\tau}, \qquad n = 1, 2, \cdots \tag{21}$$

In this paper, we define the reciprocal of the observation time interval τ between two overlapping CCDs as the **Characteristic Frequency** of this pair of CCDs, so the characteristic frequency F can be written as:

$$F = \frac{1}{\tau} = \frac{1}{T_r \times L} \tag{22}$$

Where T_r denotes the image line time, and L represents the row interval between the two overlapping CCDs. Substitute Eq. (22) into Eq. (21), the blind frequencies can be expressed as:

$$f_k \neq n \cdot F, \qquad n = 1, 2, \cdots \tag{23}$$

Therefore, the jitter at integer multiples of the characteristic frequency cannot be detected from the images of the pair of CCDs.

In addition, according to Eq. (20), the error transfer coefficient of the amplitudes between the offset and jitter can be expressed as:

$$\delta' = \left| \frac{1}{2\sin\left(\pi \cdot \tau \cdot f_k\right)} \right| \cdot \delta \tag{24}$$

Where δ and δ' denote the errors of the offset and the jitter, respectively. In the cases where the frequency is close to an integer multiple of the characteristic frequency F, the frequency f_k can be written as:

$$f_k = \left(n + \Delta n\right) \cdot F, \qquad \Delta n \to 0 \tag{25}$$

The error transfer coefficient of the amplitudes at the frequency f_k can be expressed as:

$$\delta' = \left| \frac{1}{2\sin\left[\pi \cdot \tau \cdot F \cdot \left(n + \Delta n\right)\right]} \right| \cdot \delta = \left| \frac{1}{2\sin\left[\pi \cdot \left(n + \Delta n\right)\right]} \right| \cdot \delta = \left| \frac{1}{2\sin\left(\Delta n \cdot \pi\right)} \right| \cdot \delta \gg 1 \cdot \delta, \qquad \Delta n \to 0 \tag{26}$$

It can be seen that, in the cases where the frequencies are close to integer multiples of the characteristic frequency, the error transfer coefficient between the offset and jitter is much larger than 1, leading to significant amplification of the error, which eventually results in a large measurement error of the jitter.

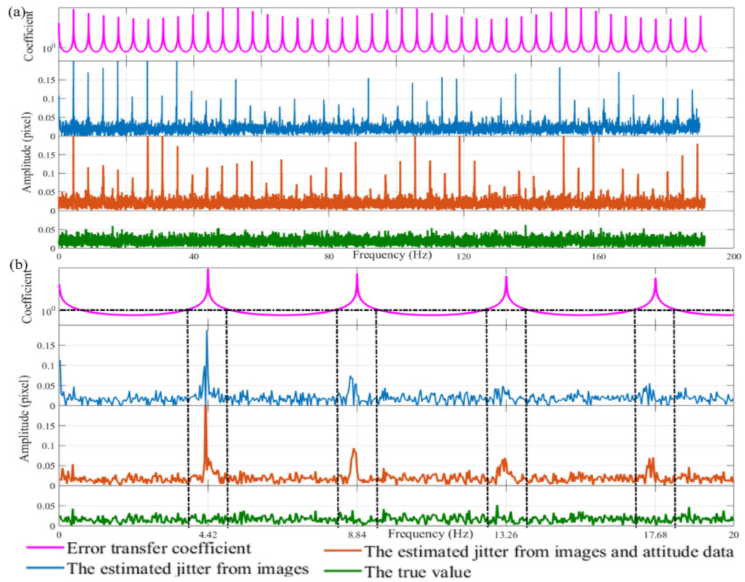

Fig. 4. Results of the numerical simulations. (a) The amplitude-frequency curves in [0 192Hz]; (b) The amplitude-frequency curves in [0 20Hz].

In order to verify the correctness of the above theoretical analysis, numerical simulations with the characteristic frequency of Chinese Heavenly Palace-1 satellite were conducted. For Chinese Heavenly Palace-1 satellite, with the image line time T_r of 65 microseconds and the row interval L of 3480 lines between two staggered CCDs, the characteristic frequency is equal to 4.42Hz according to Eq. (22). Theoretically, the frequencies equal to integer multiples of 4.42Hz cannot be detected, and the measurement error increases significantly at the frequencies near integer multiples of 4.42Hz. Theoretically, the parallax observation images can detect the highest frequency of jitter up to $1/(2u \times T_r)$ [37], with the sampling interval u of 40 lines, the maximum detectable frequency is expected up to 192Hz ($1/(2u \times T_r) = 1/2/40/65\mu s = 192$Hz). So a band-limited white noise within [0 192Hz] was used to simulate the true jitter. The results are shown in Fig. 4, where the green curves, red curves, blue curves and purple curves represent the true jitter, the jitter results from the proposed method, the jitter results from the existing method and the error transfer coefficient, respectively. Large numbers of peaks appear in both the methods' results, and they are all located at the frequencies where the corresponding error transfer coefficients are greater than 1, as shown in Fig. 4(a), in contrast, at the frequencies where the corresponding error transfer coefficients are lower than 1, the amplitudes from both the methods are basically consistent with the truth value, as shown in Fig. 4(b). The phenomenon confirmed that, just like the existing method based on parallax observation images, the proposed method cannot detect the jitter frequencies at integer multiples of the characteristic frequency. Moreover, the jitter measurement error near integer multiples of the characteristic frequency is amplified significantly. However, outside the above blind bands, the frequencies are detectable.

Therefore, for the jitter extracted from parallax observation images, not only the frequencies at integer multiples of the characteristic frequency cannot be detected, but also the measurement error near integer multiples of the characteristic frequency is amplified significantly. But, it should be emphasized that these frequencies, whose corresponding error transfer coefficients lower than 1, are detectable.

4.2 Analysis of jitter detection accuracy

The measurement accuracy of jitter detection depends on the error of the offset and low-frequency jitter derived from attitude data. Numerical simulations were conducted to determine how the measurement accuracy varies with its offset data error and low-frequency jitter error.

Since the highest detectable frequency is theoretically up to 192Hz for Chinese Heavenly Palace-1 satellite, we simulated the jitter by using a sine function whose frequency was a random number between 0 and 192Hz, and then sample it every 512ms to form a low-frequency jitter data. The corresponding offset data was calculated by using Eq. (2), where the interval R was set to 87 (consistent with Section 5.2). Following this, the offset and low-frequency jitter data were mixed with white noise σ_{offset} and σ_{low}, respectively. Initial jitter was then estimated according to Eq. (11), consequently calculating the global jitter by the use of Eq. (7).

For each value of σ_{offset} and σ_{low}, a hundred simulations were repeated. In each simulation, the deviation between the estimated jitter and its true value was employed to calculate its root-mean-square error (RMSE). Thus, a hundred RMSE data was then obtained, and the mean value of the 100 RMSE data was used to evaluate the performance of the proposed method.

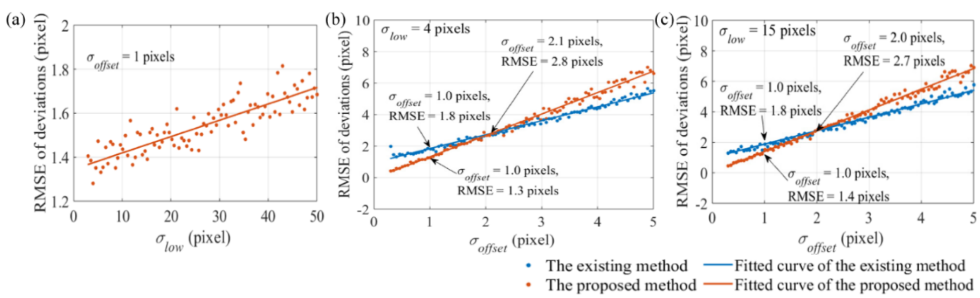

Fig. 5. Relationships between the RMSE of jitter detection and white noise mixed in (a) low-frequency jitter when σ_{offset} = 1 pixels; (b) offset data when σ_{low} = 4 pixels (cross-track direction); (c) offset data when σ_{low} = 15 pixels (down-track direction).

Figure 5 shows how the RMSE vary with σ_{offset} and σ_{low}. Just like the existing method, the proposed method's RMSE also increases with offset's white noise σ_{offset}, and compared with the white noise σ_{low} added into low-frequency jitter derived from attitude data, offset's white noise σ_{offset} seems to have a more significant impact on the proposed method's RMSE, although they both increase the proposed method's RMSE. For Chinese Heavenly Palace-1 satellite, its attitude data accuracy was 0.0002 degrees, equivalent to a cross-track displacement of about 4 pixels and a down-track displacement of 15 pixels (provided by Changchun Institute of Optics, Fine Mechanics and Physics), so we simulated the relationship between RMSE and σ_{offset} when σ_{low} is equal to 4 pixels and 15 pixels, corresponding to the cross-track and down-track directions, respectively. In the cross-track direction, when σ_{offset} is lower than 2.1 pixels, the proposed method can reach higher accuracy than the existing method dose, as shown in Fig. 5(b). Similarly, in the down-track direction, when σ_{offset} is lower than 2.0 pixels, the proposed method can be more accurate than the existing method, as shown in Fig. 5(c).

The accuracy of offset depends on the image quality, image contents and image matching method, which can generally reach pixel or even sub-pixel level. When the offset' accuracy σ_{offset} is 1 pixel, the proposed method's RMSE can reach 1.3 pixels for the cross-track direction, and 1.4 pixels for the down-track direction, while the existing method's RMSE can reach 1.8 pixels, as shown in Table 1. Compared with the attitude data with an accuracy of

0.0002 degrees and the existing method with an accuracy of 1.8 pixels, the proposed method may be more accurate for Chinese Heavenly Palace-1 satellite.

Table 1. Accuracy of three methods

Method based on	Accuracy at **offset error = 1 pixel**	
	Cross-track direction	Down-track direction
Attitude data	**4 pixels**	**15 pixels**
Parallax observation images	**1.3 pixels**	**1.4 pixels**
Parallax observation images + Attitude data	**1.8 pixels**	**1.8 pixels**

Therefore, the offset error is the main factor for the proposed method's accuracy. In the cases with offset error of pixel-level or even sub-pixel level, the proposed method may provide more convincing results than the existing method and attitude data.

5. Experiments and results discussion

5.1 Study area and image sources

The Chinese Heavenly Palace-1 satellite, which was launched on September 29, 2011, carries a visible light camera (VLC), the VLC is composed of five panchromatic CCD arrays on the focal plane, as shown in Fig. 6. Two adjacent CCDs overlap each other by 40 columns of pixels. The distance between two adjacent CCDs is 3480 lines, and the image line time is typically about 65 microseconds depending on the orbital altitude. So the overlapping CCDs shoot the same ground target with a time interval of about 226.2 milliseconds.

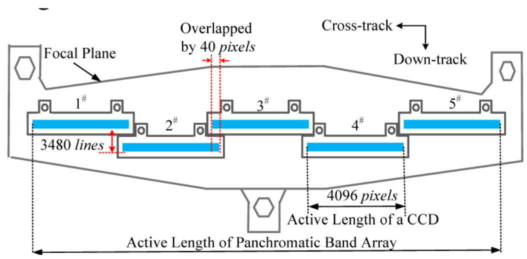

Fig. 6. Layout of the focal plane of the VLC on Chinese Heavenly Palace-1 satellite (not to scale).

It should be noted that, in focal plane coordinate system $O(x, y)$, the image motion velocity varies with x and y. Figure 7 illustrates its spatial distribution on focal plane. Theoretically, the line time of each CCD should be set to the same value as the image motion velocity of its own position, instead, VLC set all the five CCDs' line time to the image motion velocity at the center of its focal plane, where CCD $3^{\#}$ was located. As a result, CCD $3^{\#}$ matched with its image motion velocity better than any other CCD did, and its image quality was also higher than others. Therefore, we select the images from CCD $3^{\#}$ and its adjacent CCD $2^{\#}$ and CCD $4^{\#}$ to detect jitter.

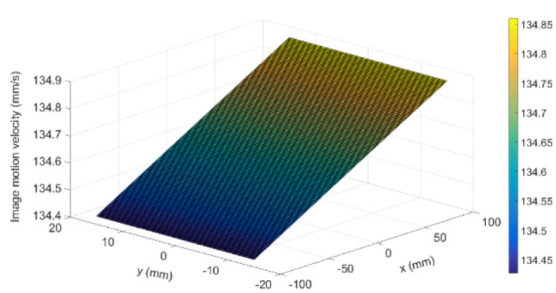

Fig. 7. Spatial distribution of image motion velocity on the focal plane when VLC was shooting the Study area A.

Figure 8 illustrates the two study areas and the scenes from CCD $2^{\#}$, CCD $3^{\#}$ and CCD $4^{\#}$ on the focal plane of VLC. The study area A, located in Beijing City, China, was imaged at 14:29 PM March 6, 2012. The study area B was located in Shanxi province, China, the corresponding images were obtained at 14:15 PM March 17, 2012.

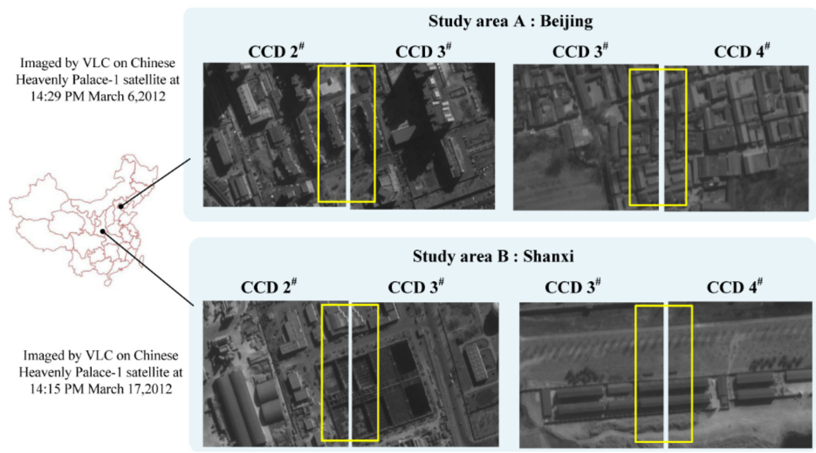

Fig. 8. Study areas and the corresponding images from CCD $2^{\#}$ (left), CCD $3^{\#}$ (middle) and CCD $4^{\#}$ (right) of the VLC on Chinese Heavenly Palace-1 satellite.

5.2 Result of jitter estimation in cross-track direction

Compared with the existing method based on parallax observation images [21], the proposed method combines the images and attitude data to detect jitter. In order to test the performance of the proposed approach, experiments on Chinese Heavenly Palace-1 data were conducted. In addition, comparisons with the on-orbit attitude data from attitude-measuring sensors and the existing method based on images were presented to demonstrate the reliability of the proposed approach in cross-track direction.

We selected two pairs of CCDs to detect jitter: CCD $2^{\#}$ and CCD $3^{\#}$, CCD $3^{\#}$ and CCD $4^{\#}$. In a shooting mission of about 30 seconds, more than 450,000 lines of images were obtained from each CCD. The images were aligned by eliminating the first 3480 lines in CCD $3^{\#}$ image and the last 3480 lines in the CCD $2^{\#}$ and CCD $4^{\#}$ images. The rest images were matched using the method in Section 3.1, and the registration points were sampled every 40 image lines, so the sampling frequency of registration points was up to 384Hz ($1/(40 \times 65\mu s) \approx 384$Hz). Reference templates are the neighborhood of 10×10 pixels around registration points and the search range was set to be 40×40 pixels. As a result, more than 11,000 offset points were acquired for each study area.

Firstly, there is a position difference of about 26.5 *mm* in the scanning direction between the CCD $3^{\#}$ and CCD $2^{\#}$ (CCD $4^{\#}$), causing an image motion speed difference, which in turn lead to a linear component in the original offset data. Therefore, it is necessary to eliminate the linear component from the original offset data. First degree polynomial fitting was performed on the original offset data, and the fitting results were eliminated from the original data. Following this, median filtering was carried out to remove glitches from the offset data after linear compensation. Figures 9(a)-9(d) illustrate the offset data $\{g(r)\}_{11276}$ from CCD $2^{\#}$ and CCD $3^{\#}$ of Study area A, CCD $3^{\#}$ and CCD $4^{\#}$ of Study area A, CCD $2^{\#}$ and CCD $3^{\#}$ of Study area B and CCD $3^{\#}$ and CCD $4^{\#}$ of Study area B, respectively. It can be seen that the linear component and glitches are effectively eliminated after linear compensation and median filtering.

Optics EXPRESS

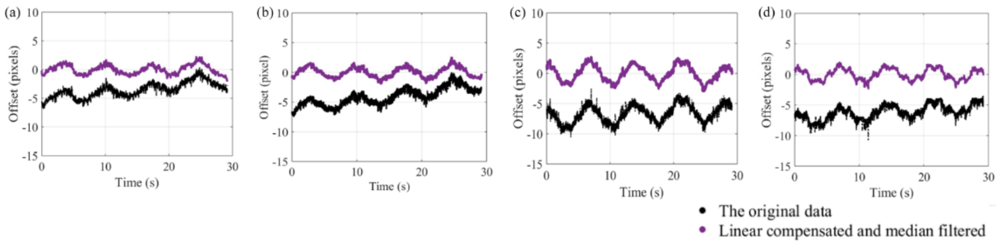

Fig. 9. Results of the cross-track offset from (a) CCD 2# and CCD 3# of Study area A; (b) CCD 3# and CCD 4# of Study area A; (c) CCD 2# and CCD 3# of Study area B; (d) CCD 3# and CCD 4# of Study area B.

Secondly, Chinese Heavenly Palace-1 satellite updated attitude data for VLC every 512 milliseconds, meaning that after a shooting mission of 30s and its 30s preparation phase, 117 attitude data samples would be acquired. Substitute all the samples into the Eq. (9) to obtain 117 points of low-frequency jitter. According to Nyquist's sampling theorem, the low-frequency jitter points contained the attitude information below 0.98Hz ($1/(512ms \times 2) \approx 0.98$Hz).

The low-frequency jitter points were fitted using the model in Eq. (10). Substitute the sampling times $\{r \times T_g\}_R$ of the offset data into the fitting function to obtain a low-frequency jitter series $\{d(r)\}_{\mathrm{R}}$, where $d(r)$ indicates the low-frequency jitter at time $r \times T_g$. In this experiments, the sampling period T_g of offset data is 2.6ms, $R = \lfloor \tau/\mathrm{T_g} \rfloor = \lfloor 226.2ms/2.6ms \rfloor =$ 87.

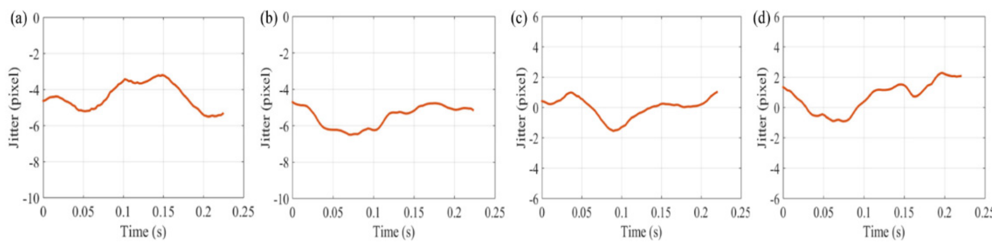

Fig. 10. Results of the cross-track initial jitter from (a) CCD 2# and CCD 3# of Study area A; (b) CCD 3# and CCD 4# of Study area A; (c) CCD 2# and CCD 3# of Study area B; (d) CCD 3# and CCD 4# of Study area B.

With the offset series and the low-frequency jitter, an objective function was established according to Eq. (11). The smoothest solution $\{j(r)\}_{87}$ that minimizes the objective function was found by using the conjugate gradient method, and $\{j(r)\}_{87}$ was regarded as the optimal solution of the initial jitter, the results from different pairs of CCDs and different study areas are shown in Fig. 10.

Thirdly, with the estimated initial jitter $\{j(r)\}_{87}$ and the offset data $\{g(r)\}_{11276}$ after linear compensation and median filtering, the jitter can be calculated according to the Eq. (7). Figures 11(a)-11(d) illustrate the estimated jitter results from CCD 2# and CCD 3# of Study area A, CCD 3# and CCD 4# of Study area A, CCD 2# and CCD 3# of Study area B and CCD 3# and CCD 4# of Study area B, respectively. The red and blue curves represent the estimated jitter from the proposed method and the existing method based on images, respectively. Direct-current component in the results was removed as we only focused on periodic motion. It can be seen that the overall trends of the two curves agree with each other basically. For the same study area, the estimated results from the pair of CCD 2# and CCD 3# are basically consistent with that from the pair of CCD 3# and CCD 4#.

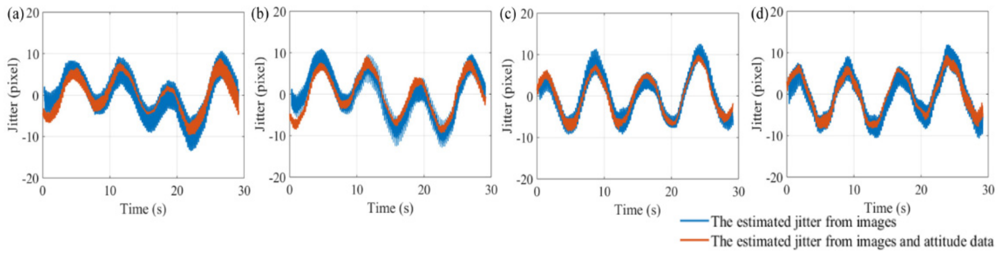

Fig. 11. Results of the total jitter in the cross-track direction from (a) CCD 2# and CCD 3# of Study area A; (b) CCD 3# and CCD 4# of Study area A; (c) CCD 2# and CCD 3# of Study area B; (d) CCD 3# and CCD 4# of Study area B.

For Chinese Heavenly Palace-1 satellite, the maximum detectable frequency is theoretically up to 192Hz (mentioned in Section 4.1). The entire theoretical bandwidth was divided into two bands as follows:

The attitude-measuring sensors equipped on Chinese Heavenly Palace-1 satellite measured rotation angle with an accuracy of 0.0002 degrees, equivalent to a focal plane displacement of about 4 pixels for the cross-track direction, and 15 pixels for the down-track direction. As a result, the corresponding low-frequency jitter derived from such attitude data has an accuracy of about 4 pixels for the cross-track direction, and 15 pixels for the down-track direction. Thus, for the cross-track direction, it is reasonable using the low-frequency jitter derived from attitude data as a reference. Since the attitude-measuring sensors supplied attitude data every 512 milliseconds, the highest frequency contained in the attitude data was nearly 0.98 Hz (1/ (512ms × 2) ≈0.98Hz). Based on this, the first band was settled as 0~0.98Hz.

To extract the low-frequency components, the total jitter results were filtered by a lowpass filter with a cutoff frequency of 0.98Hz. Figures 12(a)-12(d) illustrate the time-domain jitter from CCD 2# and CCD 3# of Study area A, CCD 3# and CCD 4# of Study area A, CCD 2# and CCD 3# of Study area B and CCD 3# and CCD 4# of Study area B, respectively. Figures 12(e)-12(h) show the frequency-domain jitter from CCD 2# and CCD 3# of Study area A, CCD 3# and CCD 4# of Study area A, CCD 2# and CCD 3# of Study area B and CCD 3# and CCD 4# of Study area B, respectively. The black dots, red curves and blue curves represent the low-frequency jitter results from attitude data, the proposed method and the existing method based on images, respectively. In the time domain, the overall trends of the three curves agree with each other basically. In the frequency domain, all peaks are located at 0.12Hz. It can be seen that, for the same pair of CCDs and the same study area, the jitter at 0.12Hz was detected by all the three approaches. Not only that, the jitter at 0.12Hz was also explored by different CCDs and different study areas, so all the results share the same main frequency, except for some slight differences in their amplitudes, as shown in Table 2. The mean value and RMSE of the amplitudes for the proposed method are 5.80 pixels and 0.31pixels, 5.47 pixels and 0.33 pixels for the existing method, and 6.29 pixels and 0.31 pixels for the low-frequency jitter derived from attitude data. It is reasonable to believe that there was the jitter at 0.12Hz with an amplitude about 6 pixels in the cross-track direction during Chinese Heavenly Palace-1 satellite shooting the above study areas.

Optics EXPRESS

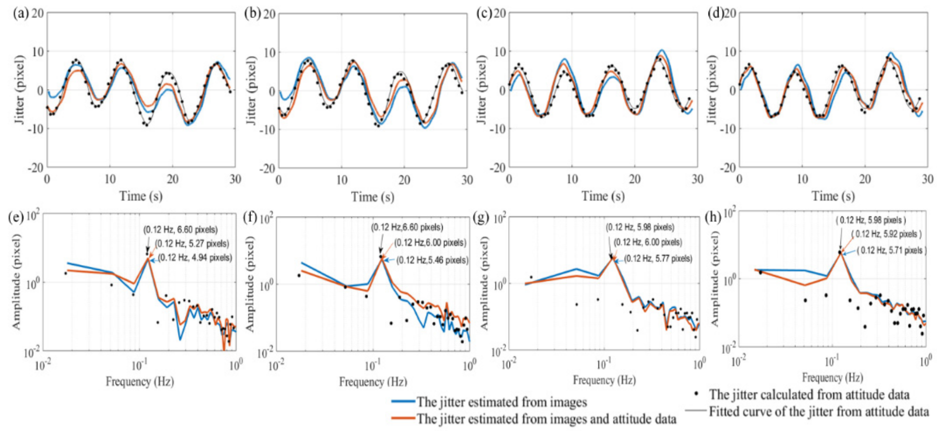

Fig. 12. Cross-track comparisons of the low-frequency jitter. Time-domain results from (a) CCD 2# and CCD 3# of Study area A; (b) CCD 3# and CCD 4# of Study area A; (c) CCD 2# and CCD 3# of Study area B; (d) CCD 3# and CCD 4# of Study area B. Frequency-domain results from (e) CCD 2# and CCD 3# of Study area A; (f) CCD 3# and CCD 4# of Study area A; (g) CCD 2# and CCD 3# of Study area B; (h) CCD 3# and CCD 4# of Study area B.

Table 2. Results of cross-track low-frequency jitter (frequency's unit: Hz, amplitude' unit: pixels).

Methods based on		Images + attitude data		Images		Attitude data	
		Frequency	Amplitude	Frequency	Amplitude	Frequency	Amplitude
Study area A	2#3#	0.12	5.27	0.12	4.94	0.12	6.60
	3#4#	0.12	6.00	0.12	5.46	0.12	6.60
Study area B	2#3#	0.12	6.00	0.12	5.77	0.12	5.98
	3#4#	0.12	5.92	0.12	5.71	0.12	5.98
Mean/ RMSE	–	**0.12/0.00**	**5.80/0.31**	**0.12/0.00**	**5.47/0.33**	**0.12/0.00**	**6.29/0.31**

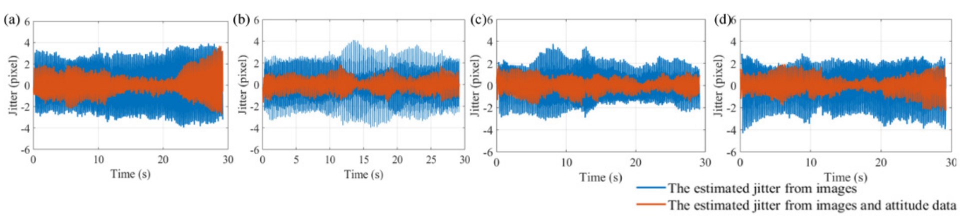

Fig. 13. Time-domain cross-track comparisons of the high-frequency jitter from (a) CCD 2# and CCD 3# of Study area A; (b) CCD 3# and CCD 4# of Study area A; (c) CCD 2# and CCD 3# of Study area B; (d) CCD 3# and CCD 4# of Study area B.

The rest frequency range from 0.98Hz to 192Hz was the second band. The jitter in this range was acquired by subtracting the above low-frequency components from the total jitter data. Figures 13(a)-13(d) and figures. 14(a)-14(d) illustrate the high-frequency time-domain jitter and the frequency-domain jitter from CCD 2# and CCD 3# of Study area A, CCD 3# and CCD 4# of Study area A, CCD 2# and CCD 3# of Study area B and CCD 3# and CCD 4# of Study area B, respectively. The red and blue curves represent the estimated jitter results from the proposed and the existing method, respectively. For the same CCD pair and study area, the jitter results from the two methods differ from each other. Not only that, the results also vary between different CCD pairs and different study areas. However, there seems to be some pattern in the frequency domain. The peaks, from different CCD pairs, different methods and different study areas, are all located around 4Hz, 8Hz, 13Hz, 17Hz, *etc*. as show in Table 3, and the peaks' frequency are approximately an arithmetic sequence. So they almost share the same peak frequencies, while the corresponding amplitudes are quite different.

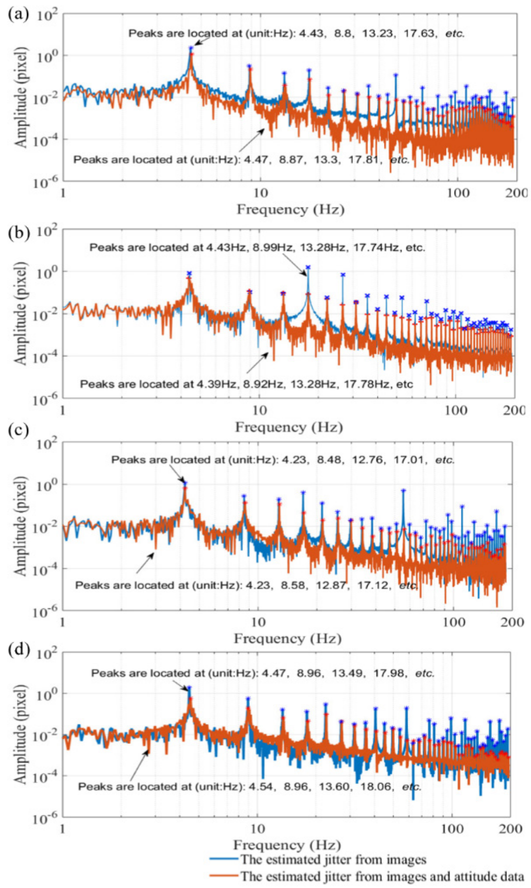

Fig. 14. Frequency-domain cross-track comparisons of the high-frequency jitter from (a) CCD 2# and CCD 3# of Study area A; (b) CCD 3# and CCD 4# of Study area A; (c) CCD 2# and CCD 3# of Study area B; (d) CCD 3# and CCD 4# of Study area B.

Table 3. Statistical results of cross-track comparisons in [0.98 192Hz]

Methods based on		Images + attitude data	Images
		Peaks' frequencies (Hz)	Peaks' frequencies (Hz)
Study area A	2#3#	4.47, 8.87, 13.30, 17.81, *etc.*	4.43, 8.80, 13.23, 17.63, *etc.*
	3#4#	4.39, 8.92, 13.28, 17.78, *etc.*	4.43, 8.99, 13.28, 17.74, *etc.*
Study area B	2#3#	4.23, 8.58, 12.87, 17.12, *etc.*	4.23, 8.48, 12.76, 17.01, *etc.*
	3#4#	4.54, 8.96, 13.60, 18.06, *etc.*	4.47, 8.96, 13.49, 17.98, *etc.*

For Chinese Heavenly Palace-1 satellite, the characteristic frequency is equal to 4.42Hz. Based on the analysis in Section 4.1, the frequencies equal to integer multiples of 4.42Hz cannot be detected from one pair of CCDs' overlapping images. Moreover, the measurement error increases significantly at the frequencies near integer multiples of 4.42Hz. This phenomenon shown in Fig. 14 confirms the existence of the blind frequencies mentioned in Section 4.1.

5.3 Result of jitter estimation in down-track direction

The attitude-measuring sensors installed on Chinese Heavenly Palace-1 satellite measured rotation angle with an accuracy of 0.0002 degrees, equivalent to a focal plane displacement of about 4 pixels for the cross-track direction, but 15 pixels for the down-track direction. Consequently, for Chinese Heavenly Palace-1 satellite, the attitude data from its attitude-measuring sensors has limited reference value for the down-track jitter comparisons.

Therefore, unlike the cross-track direction, the down-track comparisons of jitter results were only conducted between the proposed method and the existing image-based method, rather than with the attitude data.

Following the same steps as the cross-track direction, we obtained four groups of down-track jitter from the two study areas and the two pairs of CCDs mentioned in Section 5.1.

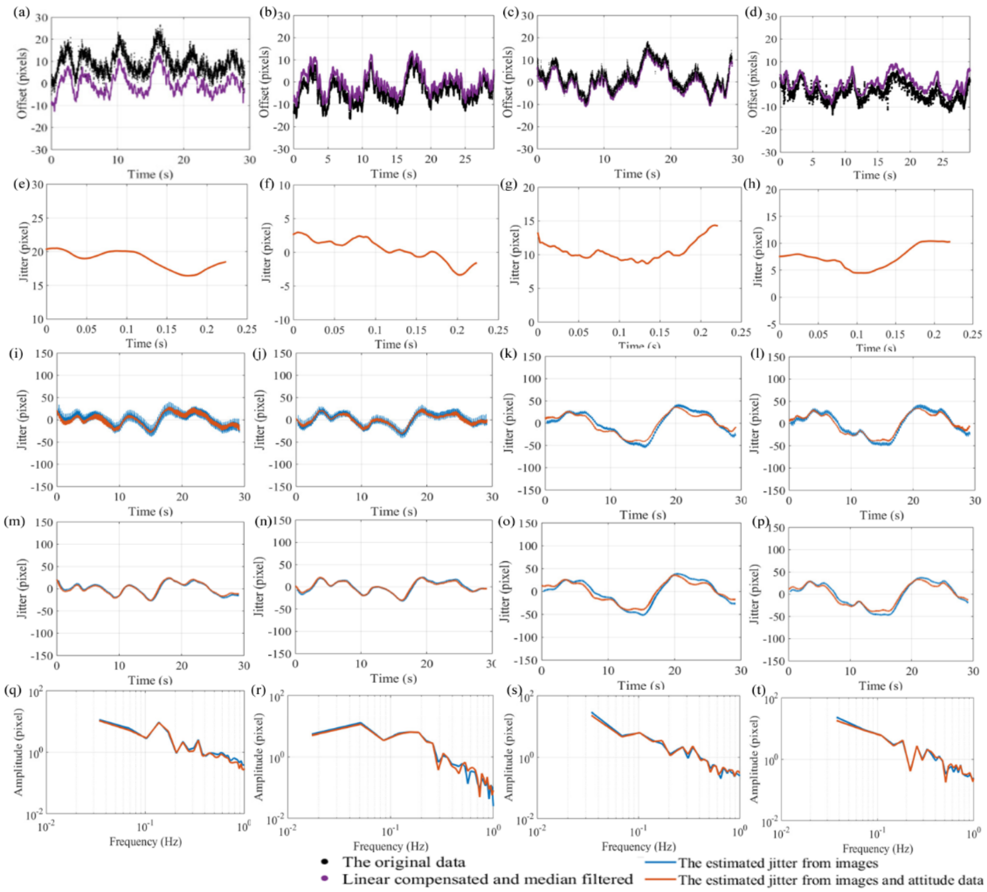

Fig. 15. Down-track comparisons between offset from (a) CCD 2# and CCD 3# of Study area A; (b) CCD 3# and CCD 4# of Study area A; (c) CCD 2# and CCD 3# of Study area B; (d) CCD 3# and CCD 4# of Study area B; Initial jitter from (e) CCD 2# and CCD 3# of Study area A; (f) CCD 3# and CCD 4# of Study area A; (g) CCD 2# and CCD 3# of Study area B; (h) CCD 3# and CCD 4# of Study area B; Total jitter from (i) CCD 2# and CCD 3# of Study area A; (j) CCD 3# and CCD 4# of Study area A; (k) CCD 2# and CCD 3# of Study area B; (l) CCD 3# and CCD 4# of Study area B; Low-frequency time-domain jitter from (m) CCD 2# and CCD 3# of Study area A; (n) CCD 3# and CCD 4# of Study area A; (o) CCD 2# and CCD 3# of Study area B; (p) CCD 3# and CCD 4# of Study area B; Low-frequency frequency-domain jitter from (q) CCD 2# and CCD 3# of Study area A; (r) CCD 3# and CCD 4# of Study area A; (s) CCD 2# and CCD 3# Study area B; (t) CCD 3# and CCD 4# Study area B.

The first band was settled as 0~0.98Hz. Figures 15(a)-15(t) illustrate the offset data, initial jitter, total jitter, low-frequency time-domain jitter, and low-frequency frequency-domain jitter from CCD 2# and CCD 3# of Study area A, CCD 3# and CCD 4# of Study area A, CCD 2# and CCD 3# of Study area B and CCD 3# and CCD 4# of Study area B, respectively. Within the low-frequency range of [0, 0.98Hz], for the same CCD pair and study area, the jitter results from the proposed method are basically consistent with that from the existing method. Likewise, those jitter from the same study area but different CCD pairs also agree with each other in general. However, large differences in jitter results are found between different study

Optics EXPRESS

areas. Moreover, unlike the cross-track direction, no significant peaks appear on any amplitude-frequency curve.

The jitter in the down-track direction is mainly caused by a satellite's pitching motion, while the cross-track jitter is caused by its rolling angle. The above cross-track jitter results show obvious periodicity, while the down-track jitter dose not. For Chinese Heavenly Palace-1 satellite, a single shooting mission can only last for 30 seconds, probably less than its pitching period, so that the estimated down-track jitter curves failed to show obvious periodicity. According to Nyquist sampling theorem, the sampling duration of a signal is too short to restore its real curve, thus the main frequency components cannot be extracted from the down-track jitters. This is why no significant peaks were found on any amplitude-frequency curve. In addition, the two study areas were shoot separately on March 6 and March 17, 2012, thus the jitter curves extracted from the two study areas are likely to be at different stages of s pitch cycle, for example, one is around the peak of a wave and the other is around the trough, which may leads to a great difference between the two jitter curves.

The rest frequency range from 0.98Hz to 192Hz was the second band, and the jitter within this band was acquired by subtracting the above low-frequency components from the total jitter data. Comparisons between the proposed method and the existing method based on images were conducted to demonstrate the performance within this band. Figures 16(a)-16(d) illustrate the high-frequency time-domain jitter from CCD 2$^{\#}$ and CCD 3$^{\#}$ of Study area A, CCD 3$^{\#}$ and CCD 4$^{\#}$ of Study area A, CCD 2$^{\#}$ and CCD 3$^{\#}$ of Study area B and CCD 3$^{\#}$ and CCD 4$^{\#}$ of Study area B, respectively. Figure 17 illustrate the high-frequency frequency-domain jitter results. The red and blue curves represent the estimated jitter results from the proposed method and the existing method based on images, respectively. Just like the cross-track direction, the two curves differ from each other in the time domain, while all the peaks from different CCD pairs, different methods and different study areas are located around integer multiples of the characteristic frequency of 4.42Hz, which further proves the existence of blind frequencies in jitter detection mentioned in Section 4.1.

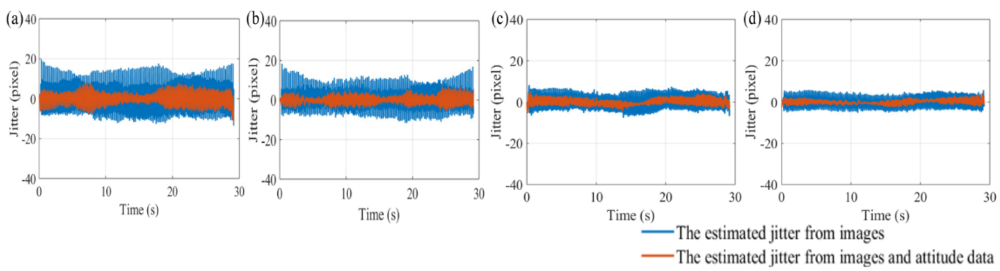

Fig. 16. Time-domain down-track comparisons of the high-frequency jitter from (a) CCD 2# and CCD 3# of Study area A; (b) CCD 3# and CCD 4# of Study area A; (c) CCD 2# and CCD 3# of Study area B; (d) CCD 3# and CCD 4# of Study area B.

Optics EXPRESS

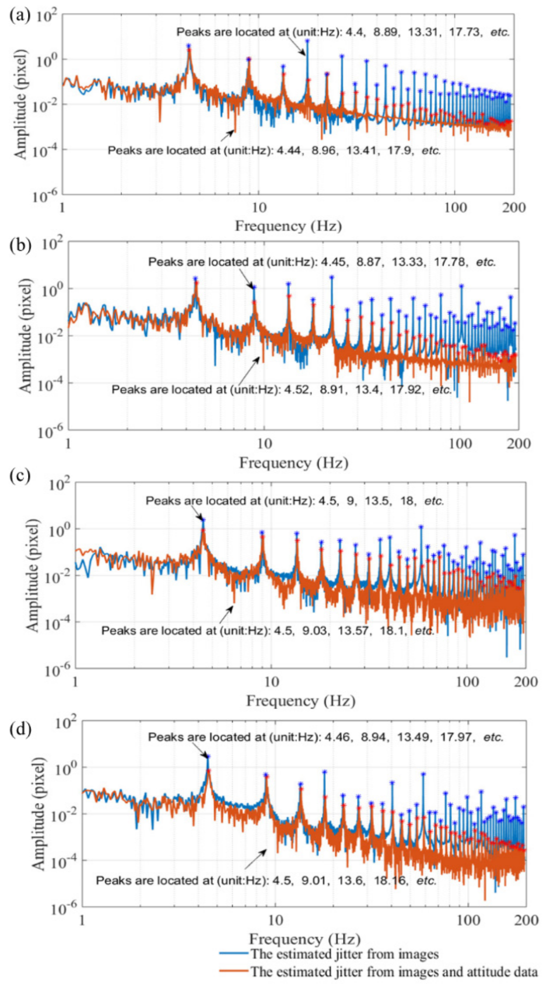

Fig. 17. Frequency-domain down-track comparisons of the high-frequency jitter from (a) CCD 2# and CCD 3# of Study area A; (b) CCD 3# and CCD 4# of Study area A; (c) CCD 2# and CCD 3# of Study area B; (d) CCD 3# and CCD 4# of Study area B.

6. Conclusion

This paper combines the parallax observation images and the low-frequency attitude data to detect jitter throughout a shooting mission, including the period without overlapping images. Experiments were performed on Chinese Heavenly Palace-1 satellite images and on-orbit attitude data to test the performance of the proposed method. Five conclusions can be made as follows.

(1) Compared with the existing method that cannot detect the initial jitter due to lack of overlapping images in the initial period of a shooting mission, the proposed method combines the parallax observation images and attitude data to enable us to calculate all the jitter of a shooting mission, including the initial jitter. Experiments show that under the assist of attitude data, the initial jitter can be estimated.

(2) In both numerical simulation and experiment results, large numbers of peaks appeared near integer multiples of the characteristic frequency of 4.42Hz. The phenomenon confirmed that, just like other methods based on parallax observation images, the proposed method cannot detect the jitter frequencies at integer multiples

of the characteristic frequency. Moreover, the jitter measurement error near integer multiples of the characteristic frequency is amplified significantly. But it should be emphasized that the frequencies outside the above blind bands are detectable.

(3) Compared with the attitude data error, offset data error has a more significant impact on the measurement accuracy of the proposed method. But it is difficult to test the exact accuracy in experiments on Chinese Heavenly Palace-1 satellite due to lack of its true value. However, large numbers of numerical simulation results show that, when offset data error is 1 pixels, the RMSE of the proposed method is 1.3 pixels for the cross-track direction and 1.4 pixels for the down-track direction. By contrast, the RMSE of the existing method based on images is 1.8 pixels. Therefore, the proposed method may provide more accurate results for Chinese Heavenly Palace-1 satellite.

(4) With respect to the cross-track direction for Chinese Heavenly Palace-1 satellite, all the experiments results performed on different pairs of CCDs and different study areas indicate that the peaks in frequency-domain are located at 0.12Hz. So they share the same main frequency with attitude data, except for some slight differences in their amplitudes: the mean value and RMSE of the amplitudes for the proposed method are 5.80 pixels and 0.31pixels, 5.47 pixels and 0.33 pixels for the existing method, and 6.29 pixels and 0.31 pixels for the attitude data. Therefore, it is reasonable to believe that there was the jitter at 0.12Hz with an amplitude about 6 pixels in the cross-track direction during Chinese Heavenly Palace-1 satellite shooting the study areas.

(5) Unlike the cross-track direction, the down-track jitter results show no obvious periodicity, leading to failure in extracting any similar frequency component from the results of different CCD pairs and different research areas. One possible explanation is that the pitching period of Chinese Heavenly Palace-1 satellite is higher than its duration of a single mission of 30 seconds. So that the sampling duration is too short to restore the real jitter. Therefore, it may not be a good solution to analyze the down-track jitter of Chinese Heavenly Palace-1 satellite by using the methods based on parallax observation images.

In summary, the proposed method combines the parallax observation images and attitude data to enable us to calculate the jitter throughout a shooting mission, including the initial jitter. But the blind frequencies do exist in all methods based on parallax observation images, and the measurement error near blind frequencies increases significantly. In our future study, it is necessary to further investigate how to eliminate the blind frequencies in jitter detection from parallax observation images.

Funding

National Natural Science Foundation of China (NSFC) (Grant No.61805001) and Natural Science Foundation of Anhui Province, China (Grant No.1808085QF218).

Acknowledgments

The authors thank the editors and the reviewers for their constructive and helpful comments, and also thank the Changchun Institute of Optics, Fine Mechanics and Physics for providing experimental image and data.

Disclosures

The authors declare that there are no conflicts of interest related to this article.

References

1. S. Roques, L. Jahan, B. Rougé, and C. Thiebaut, "Satellite attitude instability effects on stereo images," in Proceedings of IEEE Conference on Acoustics, Speech and Signal Processing (IEEE, 2004), pp.iii.

2. H. Liu, D. Yan, and D. Wang, "Space camera image motion model analysis caused by spacecraft vibration," Acta Opt. Sin. **34**(6):0612001–1-0612001–5 (2014).
3. H. Liu, S. Xu, and D. Wang, "Space camera image motion measurement based on images from time delayed integration sensors overlapped area," Acta Opt. Sin. **34**(2): 0212001–1-0212001–7(2014).
4. M. Wang, C. Fan, J. Pan, S. Jin, and X. Chang, "Image jitter detection and compensation using a high-frequency angular displacement method for Yaogan-26 remote sensing satellite," ISPRS J. Photogramm. Remote Sens. **130**, 32–43 (2017).
5. H. L. Haiqiu Liu, D. W. Dong Wang, D. Y. Dejie Yan, and S. X. Shuyan Xu, "Study on blind band elimination in jitter estimation," Chin. Opt. Lett. **12**(10), 101203 (2014).
6. V. Amberg, C. Dechoz, L. Bernard, D. Greslou, F. de Lussy, and L. Lebegue, "Inflight attitude perturbances estimation: application to PLEIADES-HR satellites," Proc. SPIE **8866**, 886612 (2013).
7. F. Ayoub, S. Leprince, R. Binet, K. W. Lewis, O. Aharonson, and J.-P. Avouac, "Influence of camera distortions on satellite image registration and change detection applications," in Proceedings of IEEE International Geoscience and Remote Sensing Symposium, (IEEE, 2008), pp. II-1072–II-1075.
8. R. Binet and L. Bollinger, "Horizontal coseismic deformation of the 2003 Bam (Iran) earthquake measured from SPOT-5 THR satellite imagery," Geophys. Res. Lett. **32**(2), 2307 (2005).
9. A. B. Ivanov and J. J. Lorre, "Analysis of Mars orbiter camera stereo pairs," in Lunar and Planetary Science Conference, (Lunar and Planetary Institute, 2002).
10. R. Kirk, E. Howington-Kraus, B. Redding, D. Galuszka, T. M. Hare, B. A. Archinal, L. A. Soderblom, and J. M. Barrett, "High-resolution topomapping of candidate MER landing sites with Mars Orbiter Camera narrow-angle images," J. Geophys. Res. Planets **108**(12), 12 (2003).
11. R. Kirk, E. Howington-Kraus, M. Rosiek, J. Anderson, B. Archinal, K. Becker, D. Cook, D. Galuszka, P. Geissler, T. Hare, I. M. Holmberg, L. P. Keszthelyi, B. L. Redding, W. A. Delamere, D. Gallagher, J. D. Chapel, E. M. Eliason, R. King, and A. S. McEwen, "Ultrahigh resolution topographic mapping of Mars with MRO HiRISE stereo images: meter-scale slopes of candidate Phoenix landing sites," J. Geophys. Res. Planets **113**, E00A24 (2008).
12. S. Mattson, M. Robinson, A. McEwen, A. Bartels, E. Bowman-Cisneros, R. Li, J. Lawver, T. Tran, K. Paris, and Lroc Team, "Early Assessment of Spacecraft Jitter in LROC-NAC," In Proceedings of the 41st Lunar and Planetary Institute Science Conference, The Woodlands, TX, USA, 1–5 March 2010.
13. A. S. McEwen, E. M. Eliason, J. W. Bergstrom, N. T. Bridges, C. J. Hansen, W. A. Delamere, J. A. Grant, V. C. Gulick, K. E. Herkenhoff, L. Keszthelyi, R. L. Kirk, M. T. Mellon, S. W. Squyres, N. Thomas, and C. M. Weitz, "Mars reconnaissance orbiter's high resolution imaging science experiment (HiRISE)," J. Geophys. Res. Planets **112**(5), E05S02 (2007).
14. H. Pan, G. Zhang, X. Tang, D. Li, X. Zhu, P. Zhou, and Y. Jiang, "Basic products of the ZiYuan-3 satellite and accuracy evaluation," Photogramm. Eng. Remote Sensing **79**(12), 1131–1145 (2013).
15. D. Poli and T. Toutin, "Review of developments in geometric modeling for high resolution satellite pushbroom sensors," Photogramm. Rec. **27**(137), 58–73 (2012).
16. B. C. Robertson, "Rigorous geometric modeling and correction of QuickBird imagery," in Proceedings of International Geoscience and Remote Sensing Symposium, (IEEE, 2003), pp.797–802.
17. P. Schwind, M. Schneider, G. Palubinskas, T. Storch, R. Muller, and R. Richter, "Processors for ALOS optical data: deconvolution, DEM generation, orthorectification, and atmospheric correction," IEEE Trans. Geosci. Remote Sens. **47**(12), 4074–4082 (2009).
18. X. Tong, Z. Ye, Y. Xu, X. Tang, S. Liu, L. Li, H. Xie, F. Wang, T. Li, and Z. Hong, "Framework of jitter detection and compensation for high resolution satellites," Remote Sens. **6**(5), 3944–3964 (2014).
19. T. Toutin, "State-of-the-art of geometric correction of remote sensing data: a data fusion perspective," Int. J. Image Data Fusion **2**(1), 3–35 (2011).
20. S. W. Lee, E. D. Skulsky, J. Chapel, D. Cwynar, R. Gehling, and W. A. Delamere, "Mars Reconnaissance Orbiter design approach for high-resolution surface imaging," in AAS Guidance and Control Conference,**113**, pp. 509–528(2003).
21. A. McEwen, M. Banks, N. Baugh, K. Becker, A. Boyd, J. W. Bergstrom, R. A. Beyer, E. Bortolini, N. T. Bridges, S. Byrne, B. Castalia, F. C. Chuang, L. S. Crumpler, I. Daubar, A. K. Davatzes, D. G. Deardorff, A. DeJong, W. Alan Delamere, E. N. Dobrea, C. M. Dundas, E. M. Eliason, Y. Espinoza, A. Fennema, K. E. Fishbaugh, T. Forrester, P. E. Geissler, J. A. Grant, J. L. Griffes, J. P. Grotzinger, V. C. Gulick, C. J. Hansen, K. E. Herkenhoff, R. Heyd, W. L. Jaeger, D. Jones, B. Kanefsky, L. Keszthelyi, R. King, R. L. Kirk, K. J. Kolb, J. Lasco, A. Lefort, R. Leis, K. W. Lewis, S. Martinez-Alonso, S. Mattson, G. McArthur, M. T. Mellon, J. M. Metz, M. P. Milazzo, R. E. Milliken, T. Motazedian, C. H. Okubo, A. Ortiz, A. J. Philippoff, J. Plassmann, A. Polit, P. S. Russell, C. Schaller, M. L. Searls, T. Spriggs, S. W. Squyres, S. Tarr, N. Thomas, B. J. Thomson, L. L. Tornabene, C. Van Houten, C. Verba, C. M. Weitz, and J. J. Wray, "The high resolution imaging science experiment (HiRISE) during MRO's primary science phase (PSP)," Icarus **205**(1), 2–37 (2010).
22. C. Latry, S. Artigues, and L. Bernard, "Attitude assessment using Pleiades HR capabilities," Int. Arch. Photogramm. Remote Sens. **39**(B1), 525–530 (2012).
23. T. Iwata, T. Kawahara, N. Muranaka, and D. R. Laughlin, "High-bandwidth attitude determination using jitter measurements and optimal filtering," in Proceedings of AIAA Guidance, Navigat.,Control Conf., 2009,pp. 7349–7369.

24. P. Sabelhaus, J. Bolek, S. Scott, E. Holmes, and R. James, "On-orbit ACDS performance of the Landsat 7 spacecraft," in Proceedings of AAS Guidance and Control (2001).
25. K. Janschek, V. Tchernykh, and S. Dyblenko, "Integrated camera motion compensation by real-time image motion tracking and image deconvolution," in Proceedings of International Conference on Advanced Intelligent Mechatronics.(IEEE, 2005), pp.1437–1444.
26. K. Janschek, V. Tchernykh, and S. Dyblenko, "Performance analysis of opto-mechatronic image stabilization for a compact space camera," Control Eng. Pract. **15**(3), 333–347 (2007).
27. V. Tchernykh, M. Beck, and K. Janschek, "Optical correlator based optical flow processor for real time visual navigation". InTech Open Access Publisher. 2007:223–236.
28. S. Mattson, A. Boyd, and R. L. Kirk, "HiJACK: Correcting spacecraft jitter in HiRISE images of Mars," Health Manag. Technol. **33**(5), A162 (2009).
29. S. Mattson, A. Bartels, and A. Boyd, "Continuing analysis of spacecraft jitter in LROC-NAC," Am. Nat. **152**(3), 321–337 (2011).
30. Y. Teshima and A. Iwasaki, "Correction of attitude fluctuation of terra spacecraft using ASTER/SWIR imagery with parallax observation," IEEE Trans. Geosci. Remote Sens. **46**(1), 222–227 (2008).
31. A. Iwasaki, "Detection and Estimation Satellite Attitude Jitter Using Remote Sensing Imagery," In Advances in Spacecraft Technologies, Hall, J., Ed., InTech: Rijeka, Croatia, **13**, 257–272 (2011)
32. R. Mumtaz and P. Palmer, "Attitude determination by exploiting geometric distortions in stereo images of DMC camera," IEEE Trans. Aerosp. Electron. Syst. **49**(3), 1601–1625 (2013).
33. Y. H. Jiang, G. Zhang, X. Tang, D. Li, and W. C. Huang, "Detection and correction of relative attitude errors for ZY1-02C," IEEE Trans. Geosci. Remote Sens. **52**(12), 7674–7683 (2014).
34. X. Tong, L. Li, S. Liu, Y. Xu, Z. Ye, Y. Jin, F. Wang, and H. Xie, "Detection and estimation of ZY-3 three-line array image distortions caused by attitude oscillation," ISPRS J. Photogramm. Remote Sens. **101**(10), 291–309 (2015).
35. X. Tong, Y. Xu, Z. Ye, S. Liu, X. Tang, L. Li, H. Xie, and J. Xie, "Attitude oscillation detection of the ZY-3 satellite by using multispectral parallax images," IEEE Trans. Geosci. Remote Sens. **53**(6), 3522–3534 (2015).
36. T. Sun, H. Long, B. C. Liu, and Y. Li, "Application of attitude jitter detection based on short-time asynchronous images and compensation methods for Chinese mapping satellite-1," Opt. Express **23**(2), 1395–1410 (2015).
37. S. Liu, X. Tong, F. Wang, W. Sun, C. Guo, Z. Ye, Y. Jin, H. Xie, and P. Chen, "Attitude jitter detection based on remotely sensed images and dense ground controls: a case study for Chinese ZY-3 satellite," IEEE J. Sel. Topics Appl. Earth Observ. **9**(12), 5760–5766 (2016).
38. J. Wang, P. Yu, and C. Yan, "Space optical remote sensor image motion velocity vector computational modeling, error budget and synthesis," Chin. Opt. Lett. **3**(7), 414–417 (2005).
39. L. Huang, T. Sun, T. Zhang, and H. You, "Application of DIROEF algorithm for noncollinear multiple CCD array stitching of the Chinese Mapping satellite 1-02," IEEE Geosci. Remote Sens. Lett. **14**(4), 519 (2017).
40. Y. C. Li, J. H. Dong, W. Li, Q. F. Guo, K. J. Wang, H. P. Wang, and W. G. Zhao, "Detailed analysis of the HIRISE FPA," Key Eng. Mater. **552**, 64–68 (2013).
41. S. Jiao and D. Fu, "An overview of the remote sensors of Chinese ZY-1 satellite: CCD camera and multi-spectral scanner," International Conferences on Info-Tech and Info-Net, (IEEE, 2001).1, pp.6–11.
42. J. Wang, P. Yu, and C. Yan, "Space optical remote sensor image motion velocity vector computation modeling," Acta Opt. Sin. **24**(12), 1585–1589 (2005).
43. W. Li, "Research on method of image motion compensation of space high resolution cameras' collecting scene agilely," University of Chinese Academy of Sciences. pp. 33–55(2012).
44. P. Schwind, R. Müller, G. Palubinskas, and T. Storch, "An in-depth simulation of EnMAP acquisition geometry," ISPRS J. Photogramm. Remote Sens. **70**, 99–106 (2012).
45. N. Venkateswaran, P. Goel, M. Siva, P. Natarajan, E. Krishnakumar, and N. Philip, "Precision pointing of imaging spacecraft using gyro-based attitude reference with horizon sensor updates," Sadhana **29**(2), 189–203 (2004).